IOP Publishing | Institute of Physics and Engineering in Medicine Physics in Medicine & Biology

Phys. Med. Biol. **61** (2016) 2283–2301 doi:10.1088/0031-9155/61/6/2283

Enhancement of chest radiographs obtained in the intensive care unit through bone suppression and consistent processing

Sheng Chen[1], Sikai Zhong[1], Liping Yao[2,5], Yanfeng Shang[3] and Kenji Suzuki[4]

[1] School of Optical-Electrical and Computer Engineering & Engineering Research Center of Optical Instrument and System, Ministry of Education, University of Shanghai for Science and Technology, Shanghai, People's Republic of China
[2] Department of Ultrasound, Xinhua hospital Affiliated to Shanghai Jiaotong University School of Medicine, People's Republic of China
[3] The Third Research Institute of The Ministry of Public Security, People's Republic of China
[4] Department of Electrical and Computer Engineering & Medical Imaging Research Center, Illinois Institute of Technology, Chicago, IL, USA

E-mail: chnshn@hotmail.com

Received 7 May 2015, revised 12 January 2016
Accepted for publication 4 February 2016
Published 1 March 2016

Abstract

Portable chest radiographs (CXRs) are commonly used in the intensive care unit (ICU) to detect subtle pathological changes. However, exposure settings or patient and apparatus positioning deteriorate image quality in the ICU. Chest x-rays of patients in the ICU are often hazy and show low contrast and increased noise. To aid clinicians in detecting subtle pathological changes, we proposed a consistent processing and bone structure suppression method to decrease variations in image appearance and improve the diagnostic quality of images. We applied a region of interest-based look-up table to process original ICU CXRs such that they appeared consistent with each other and the standard CXRs. Then, an artificial neural network was trained by standard CXRs and the corresponding dual-energy bone images for the generation of a bone image. Once the neural network was trained, the real dual-energy image was no longer necessary, and the trained neural network was applied to the consistent processed ICU CXR to output the bone image. Finally, a gray level-based morphological method was applied to enhance the bone

[5]Author to whom any correspondence should be addressed.

image by smoothing other structures on this image. This enhanced image was subtracted from the consistent, processed ICU CXR to produce a soft tissue image. This method was tested for 20 patients with a total of 87 CXRs. The findings indicated that our method suppressed bone structures on ICU CXRs and standard CXRs, simultaneously maintaining subtle pathological changes.

Keywords: Intensive care unit, bone suppression, artificial neural network

(Some figures may appear in colour only in the online journal)

1. Introduction

Chest radiographs (CXRs) are by far the most commonly used diagnostic imaging modalities for the identification of chest diseases such as lung cancer, tuberculosis, pneumonia, pneumoconiosis, and pulmonary emphysema. CXR is the most cost-effective, routinely available, and dose-effective diagnostic tool. It even has the ability to reveal certain unsuspected pathologic alterations (Murphy *et al* 1995). In the intensive care unit (ICU), routine CXRs are somewhat valuable in the treatment decision-making process (Chahine-Malus *et al* 2001). Clinical evaluation strongly relies on portable CXRs (Strain *et al* 1985, Wandtke 1994). Successive diagnostic images obtained using a portable computed radiography (CR) system or a digital radiography (DR) system are helpful tools for detecting significant pathological changes (Ely *et al* 2001, Amorosa *et al* 2013) such as a collapsed lung, pneumothorax, congestive heart failure, and improper tube placement within the patient (Reyes *et al* 2001, Mercan and Celebi 2014).

Although portable CXRs are widely used in the ICU to detect pathological changes, the incidence of overlooks is relatively high (Hammon *et al* 2014). Exposure settings or patient and apparatus positioning limit the accuracy of image comparison in the ICU, even for those images obtained from the same patient over short treatment intervals. This restricts the ability of clinicians to identify subtle changes that can be highly significant. Figure 1 shows some CXRs obtained for a typical ICU patient. A study of these images revealed that original ICU CXRs show low contrast and are different from each other even if they are obtained from the same patient. The image in figure 1(a) shows no congestive heart failure (CHF), while those in figures 1(b) and (c) show mild and moderate CHF, respectively. Therefore, clinicians can barely detect subtle changes on original ICU CXRs. A consistent processing method for such images is thus required such that the normal tissues in the processed image have similar intensity, contrast, and frequency signal to each other and to the standard CXR, and the abnormal tissue and pathological changes are signalized.

Currently, one of the primary methods used for processing portable CXRs is the allocation of output dynamic ranges and the display of clinically important input pixel values. The process of selecting the relevant sub-range of input pixel values and constructing an appropriate mapping function from the input pixel values to the output display media is referred to as tone-scale adjustment. Using a tone-scale method for CR images provides an optimal processing result. Some other methods also lead to improved contrast enhancement on diagnostic images(Chen and Zou 2009). However, because these methods are based on a single image, they cannot address the problem of inconsistency between images of the same patient obtained at different time points and between these images and standard CXRs. Furthermore, the application of such tone-scale techniques is not likely to provide consistent processing results, which makes it difficult for the ICU clinician to access changes accurately.

In this paper, we present a region of interest (ROI) based look-up table (LUT) (Ryoo *et al* 2013) method to enhance original ICU CXRs. With this method, the normal tissue in the processed ICU

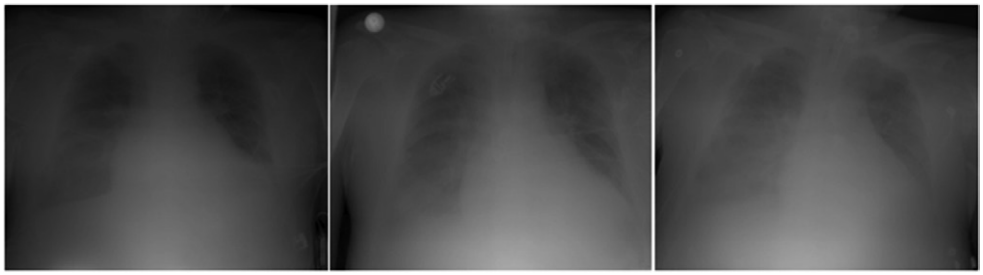

Figure 1. Some CXRs from a same patient in ICU: (a) no CHF; (b) mild CHF; (c) moderate CHF.

CXR appears consistent with that in the standard CXR, e.g. in terms of intensity and contrast. Furthermore, images obtained for the same patient are also consistent with each other and facilitate the detection of subtle pathological changes. To make diagnosis easier, the bone structures on the consistent processed image are suppressed. Some researchers have performed dedicated studies on bone suppression on CXRs. Suzuki *et al* first developed a supervised image-processing technique for separating the ribs from the soft tissue on CXRs using a multi-resolution massive-training artificial neural network (MTANN) (Suzuki *et al* 2004, 2006), a type of pixel-based machine learning (Suzuki 2012) that is considered as a supervised, highly nonlinear filter based on artificial neural network regression. Real dual-energy images were used as teaching images for training of the multi-resolution MTANN, following which the real dual-energy images were no longer necessary. An observer performance study with 12 radiologists demonstrated that the suppression of bony structures on CXRs improved the diagnostic performance of radiologists with regard to the satisfactory detection of lung nodules (Oda *et al* 2009). Plourde *et al* proposed a semi-automated technique for detecting complete scoliotic rib borders from posterior-anterior chest radiographs using an edge-following approach with multiple-path branching and oriented filtering (Plourde *et al* 2012). Ahmed *et al* presented a technique based on independent component analysis for the suppression of posterior ribs and clavicles in order to enhance the visibility of nodules and aid radiologists during the diagnosis process (Ahmed and Rasheed 2007). Loog *et al* proposed a supervised filter learning technique for the suppression of ribs (Loog *et al* 2006). The procedure is based on K-nearest neighbor regression, which incorporates knowledge obtained from a training set of dual-energy radiographs with their corresponding subtraction images for the construction of a soft-tissue image from a previous, unseen, single, standard chest image. Hogeweg *et al* presented a method for translucent elongated structure suppression on CXRs. The focus is on elongated structures, which allows the extraction of an intensity model of a structure of interest using local information only. The model is created from profiles sampled perpendicular to the structure. Profiles containing other structures are detected and eliminated to decrease the influence on the model (Hogeweg *et al* 2013). In these methods, MTANN was able to separate the ribs from the soft tissue on CXRs; however, rib edges, ribs close to the lung wall, and the clavicles were not completely suppressed. Chen *et al* proposed a specific MTANN combined with total variation (TV) for bone suppression (Chen and Suzuki 2014). Soft tissue CXRs can aid ICU clinicians in detecting subtle pathological changes as well as for radiologists in detecting lung nodules (Chen and Suzuki 2013).

In this study, we developed a bone suppression technique (Chen and Suzuki 2014) and applied it to suppress the bones on ICU CXRs. However, the ICU CXRs were often hazy and showed low contrast and increased noise. They were different from the standard CXRs. Furthermore, there were different types of fusion area within the lung field on ICU CXRs, and the traditional histogram matching

method would make the intensity and contrast of normal tissues different between ICU CXRs and standard CXRs. The consistent processing method was applied to ICU CXRs to ensure their consistency with training standard CXRs in terms of the separation between normal and abnormal tissues. The first step of this consistent processing method was background segmentation over all the images. Then, an ROI containing tissue regions that were critical for clinicians to achieve an accurate diagnosis was automatically located. Next, an LUT was constructed for each gray value in the ROI. Finally, a toe-shoulder construction step was employed to construct an LUT for very dark and light regions. In the LUT mapping step, the gray values of the pixels in the input images were mapped to the corresponding gray values in the output images. After consistent, processed ICU CXRs were obtained, they were inputted to the trained MTANN to obtain the bone images. Although the improved MTANN can derive a bone image with a high signal noise ratio (SNR) for the consistent, processed ICU CXRs, some amount of noise remains in the output bone image, because the image quality of the original ICU CXR is poor. A post-processing method based on gray-level morphological algorithm was applied to enhance the bone structure and decrease the noise in the bone image. Finally, the enhanced bone image was subtracted from the ICU CXR to obtain a consistent, processed, soft tissue image.

2. Materials and method

2.1. Database

The Kodak CR 400 system (Kodak Health Imaging Sciences, Rochester, NY) was used in our study conducted at Xinhua Hospital, Shanghai, China. In Kodak CR systems, the exposure index (EI) related to the logarithm of the incident exposure. In our study, the kVp, mAs and EI values were 80, 1.4, and 1770 respectively.

In our experiment, an anti-scatter grid was not used. Grid usage in portable radiography is often sporadic and inconsistent. From the perspective of the radiographic technologist, using grids for portable exams involves a variety of time-consuming workflow implications. These include attaching and detaching the add-on grids to the x-ray cassettes; the stringent requirements to properly position and align the x-ray source relative to the cassette behind the patient to avoid grid cutoff; the increased probability that repeated exposures will be required due to grid-cutoff artifact; and more. In addition, there is the misperception that grids are not required in digital radiography because increasing the exposure can overcome the scatter-noise level, and that image processing adjustments, such as window and level manipulations, can sufficiently compensate for the quality losses that are introduced by scattered radiation. With all of these considerations in mind, there would seem to be little motivation for the technologists to use grids in portable DR.

Direct exposed raw images were acquired without any gray-scale manipulation or preprocessing for optimization of the gray-scale processing algorithms. The results were compared to those obtained with Kodak's tone-scale algorithm.

Eighty-seven portable CXRs were collected from 20 patients using the Kodak CR 400 system. Two to nine images with a size of 2500 $\times$ 2048 pixels were obtained for each patient. The gray scale was 12 bits and the pixel size was 0.171 $\times$ 0.171 mm. Chest radiologists reviewed all the images and provided a diagnosis that included the type of disease, such as cardiomegaly, CHF, endotracheal tube, feeding tube, nasogastric tube, and ventricular assist device. Table 1 summarizes the database used in this study.

Another database comprising nine posterior-anterior standard CXRs acquired using a CR system with a dual-energy subtraction unit were used for training the improved MTANN. The dual-energy subtraction unit employed a single-shot dual-energy subtraction technique, where a single exposure that is detected by two receptor plates separated by a filter is used for obtaining images at two different energy levels (Ishigaki *et al* 1986, 1988, Stewart and Huang 1990).

Table 1. Information of the study patients.

Patient ID	Number of images	Cardiomegaly	CHF	Endotracheal Tube	Feeding Tube
1	5	No	Yes	No	Yes
2	2	Yes	Yes	No	yes
3	4	No	Yes	Yes	Yes
4	4	No	Yes	Yes	Yes
5	4	Yes	Yes	Yes	No
6	7	No	No	No	Yes
7	9	No	Yes	Yes	Yes
8	3	No	No	Yes	no
9	3	No	No	Yes	No
10	3	Yes	No	No	No
11	4	Yes	Yes	No	Yes
12	3	Yes	Yes	No	No
13	3	No	Yes	Yes	Yes
14	4	Yes	Yes	No	Yes
15	2	No	No	Yes	No
16	6	No	Yes	Yes	Yes
17	3	No	Yes	no	No
18	9	No	Yes	No	Yes
19	4	No	Yes	No	No
20	5	No	No	Yes	Yes

2.2. Scheme for original ICU CXR enhancement

Figure 2 shows our scheme for ICU CXR enhancement with bone suppression, which included four major steps. The first was consistent processing and enhancement for ICU CXRs from the same patient, which has two purposes: facilitate the easy detection of subtle pathological changes and achieve the efficiency pattern features for bone suppression, similar to those on the standard CXRs used for training. The second step involved bone image creation based on the trained MTANN, followed by bone image enhancement through the use of gray level-based morphological algorithms as the third step and soft tissue CXR creation as the fourth.

2.3. Consistent processing for CXRs

We used an ROI-based LUT method to enhance original ICU CXRs, which ensured consistency of the normal tissues in the processed ICU CXRs with those in the standard CXRs. Furthermore, images of the same patient are consistent with each other in terms of intensity and contrast. This aids clinicians in detecting subtle pathological changes. We first segmented the background, which typically corresponded to the highest signal levels in the image, where the unobstructed radiation hit the imaging plate.

For ICU CXRs, the position of the ROI, which is necessary for clinical diagnoses, varies. The basic principle of automated ROI selection is to simply identify the ROI in each image automatically. ROI identification on an image on the basis of key features (lung line, spine line) allows the correlation of two or more images. Figures 3(a) and (b) show two original ICU CXRs of the same patient, with two automatically selected ROIs (blue trapezoid). These figures show that the position of the ROI is different among images, even though they belong to the same patient.

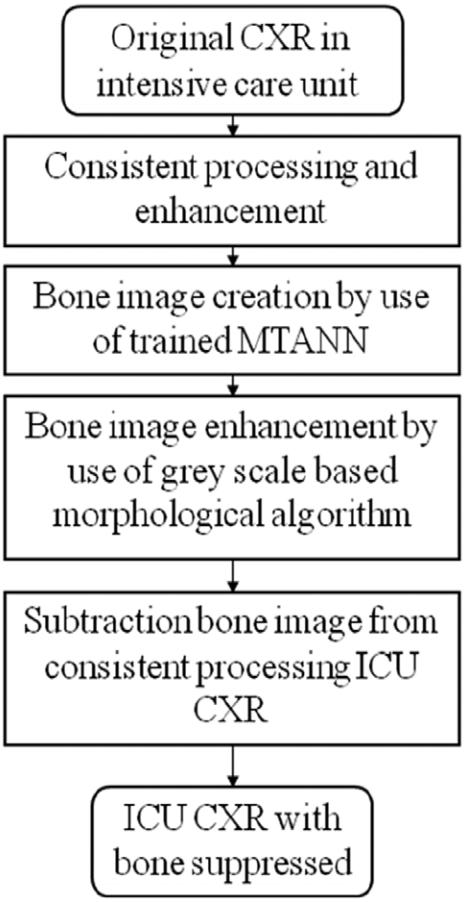

Figure 2. Main diagram of our ICU CXR enhancement scheme.

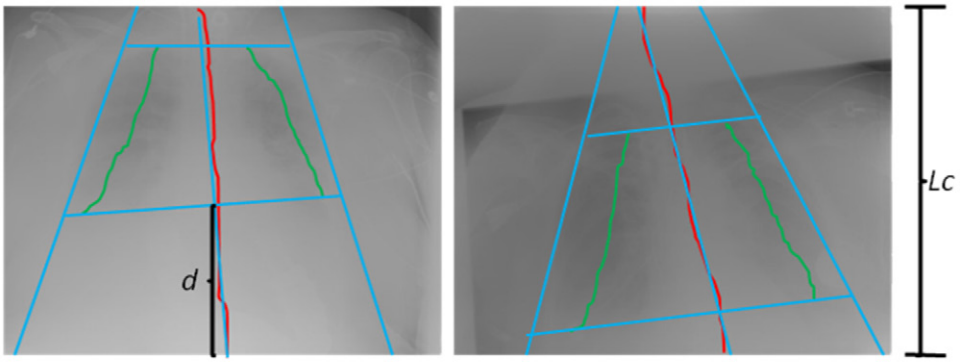

Figure 3. ROI is automatically identified by use of the key features (spine line identified by red line, lung line identified by green line, ROI identified by blue trapezoid).

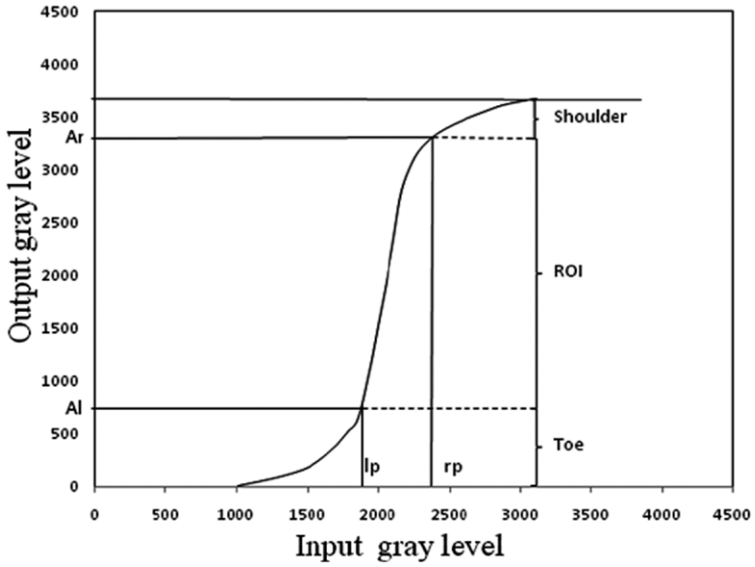

Figure 4. An example of lookup table construction, each image has a mapping curve.

In this step, the image was resized smaller. The resized image was used only for ROI selection in order to improve the speed. The pixel value for each row was assessed to determine the local maximum near the mediastinum area, and these maximum points along each row were grouped together to form the spine line, shown in figure 3 (red line). The local minimum points on both sides of the spine line were identified as candidate points for the lung line. These candidate points were grouped together, and the longest groups in the middle were chosen as the initial lung lines. Removal of the points at both ends with high pixel values further cleaned the lines. The resulting lung lines are shown as the left and right green lines in Figure 3. Once the approximate lung line and spine line were determined, a spine-line-fitting step could be executed following which we could obtain a trapezoid ROI for all images of the same patient using the spine line and the distance from the spine line to the lung line.

Then, the LUT was constructed for these ROIs. First, we identified the primary area on the image from the histogram that was calculated using the ROI only. *lp* and *rp* are gray values representing the left and right points of the histogram, respectively. The main range (5%–95%) in the ROI was achieved between the left and right points. The objective of the next few steps was to map the left point *lp* and the right point *rp* to the corresponding gray values *Al* and *Ar*.

Figure 4 shows an example of LUT construction. *lp* and *rp* are mapped to *Al* and *Ar* in the output image predefined for the same patient. However, the ROI contains the lung and spine, and the gray values of most pixels in the ROI are lower than those of the pixels in the bottom part of the image. On the other hand, the gray values of most pixels in the abdomen area are larger than *Ar*, and are mapped to the gray value between *Ar* and 4095. If *Ar* is too large, the range of [*Ar*, 4095] will be narrow. After mapping, the abdomen appears bright and the contrast is suppressed. During clinical examination, the portion of the abdomen in the image was generally different. For example, the diaphragm in figure 3(a) is higher than that in figure 3(b). If we set the same value of *Ar* for the two images, the abdomen's contrast observed in figure 3(a) was suppressed after processing. To accommodate the differences in the images due to patient positioning, the value of *Ar* should be adjusted for each image based on the ROI's position. This difference can be best expressed in terms of the ratio of the distance *d* to the column length L_c, as illustrated in figure 3. A larger d/L_c value represents a higher

percentage of the abdomen in the image, while Ar should be lowered to provide a sufficient range to map the pixels with large gray values.

Based on these considerations, Ar was adjusted using the following equation:

$$Ar = t \cdot Ar_{\mathrm{st}} + (1-t)Ar_{\mathrm{st}} \cdot (d_{\mathrm{st}}/d), 0 \leqslant t \leqslant 1, \tag{1}$$

where d is illustrated in figure 3 and d_{st} is measured for the standard CXRs used for training. The parameter t can be adjusted depending on whether the focus is primarily on image processing or on consistency. If $t = 1$, Ar is the same for the standard CXRs. If $t = 0$, each image has a different Ar value. For the images in our experiment, the gray value ranged from 0 to 4095 and t was set to 0.5 for those ICU CXRs.

Because pixels with gray values of lp are usually in the lung field of the ROI, and because of inhalation and exhalation movements and the pathological impact on the lungs, the gray value of lp for different images should not be mapped to the same Al. For example, there are two images, one obtained during inhalation and the other during exhalation, for the same patient. The lung will look darker in the inhalation image than in the exhalation image. Therefore, we should identify criteria that will not vary after the image is mapped and use them to calibrate the gray value of Al for each image. The density of the spine will not vary when routine radiographs are obtained. Therefore, Al was adjusted using the following equation:

$$\begin{aligned} &p\mathrm{dark} = \frac{\overline{rp - lp}}{spdv - spuv} \\ &Al = Al_{\mathrm{st}} + \max(a_1, \min(a_2 \cdot (p\mathrm{dark} - a_0), a_4)), \end{aligned} \tag{2}$$

where $spdv$ and $spuv$ represent the main gray-level range in the spinal region (10%–80%), which can be automatically detected, and do not depend on the patient's status.

For the images in our experiment, Al_{st} was used for the trained standard CXRs, with $a_1 = -250$, $a_2 = -300$, $a_0 = 1.8$, and $a_4 = 250$. These are empirical parameters determined from the nine training standard CXRs and validated by a radiologist. The value of Al can be justified by the $p$dark ratio for each image. For example, if the $p$dark of one image is larger than those of other images, the lung will appear darker on this image than on other images after mapping.

After we obtained lp, rp, Al, and Ar for each image, LUT construction between lp and rp to Al and Ar was applied. The mapping from [lp, rp] to [Al, Ar] was established on the basis of an active rate calculated using equation (3).

$$\begin{aligned} &\mathrm{Activity}\,[k] = \frac{\sum\limits_{(i,j)\in \mathrm{ROI}, \mathrm{img}(i,j)=k} \sum\limits_{u=i-3}^{i+3} \sum\limits_{v=j-3}^{j+3} H(u,v,i,j)}{h(k)} \\ &\mathrm{if}, hl \leqslant \left|\mathrm{img}(i,j) - \mathrm{img}(u,v)\right| \leqslant hr, H(u,v,i,j) = 1 \\ &\mathrm{else}, H(u,v,i,j) = 0 \\ &\mathrm{ActNor}\,[i] = \frac{\ln\left(\frac{\sum\limits_{i=-t}^{t} \mathrm{Activity}[i+t] \cdot h[i+t]}{\sum\limits_{i=lp}^{rp-1} h[i]} + 1\right) + 1}{\sum\limits_{i=lp}^{rp-1} \left(\ln\left(\frac{\sum\limits_{i=-t}^{t} \mathrm{Activity}\,[i+t] \cdot h[i+t]}{\sum\limits_{i=lp}^{rp-1} h[i]} + 1\right) + 1\right)}, \end{aligned} \tag{3}$$

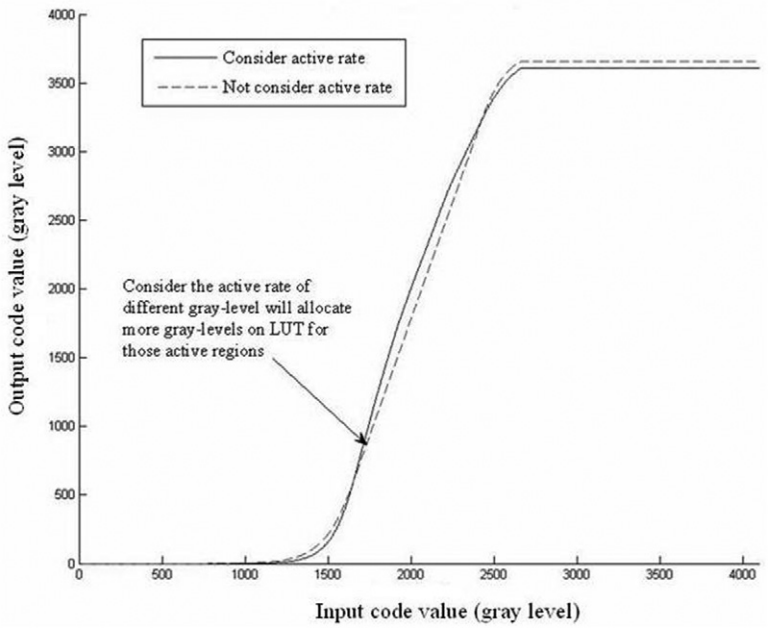

Figure 5. Active-rate considering in LUT construction, bigger slope for LUT at higher active-rate gray value.

where activity[k] is the activity at intensity k, and $h[k]$ is the number of pixels at intensity k. In our experiment, hl and hr were thresholds and were set to 50 and 1000, respectively.

$$\begin{aligned}&\mathrm{LUT}(lp) = Al\\&\mathrm{LUT}(i+1) = \mathrm{LUT}(i) + \mathrm{ActNor}(i)(Ar - Al)\mathrm{ratio},\\&+\left(\frac{(Ar - Al)(1 - \mathrm{ratio})}{rp - lp}\right)\\&0 \leqslant \mathrm{ratio} \leqslant 1\end{aligned} \tag{4}$$

In equation (4), if ratio = 0, the LUT is considered a linear mapping of [*lp, rp*] to [*Al, Ar*]. If ratio = 1, the active rate at each gray value is considered. Figure 5 shows an example of LUT construction using equation (4) considering the active rate by fixing ratio to be 0.5. This figure indicates that the slope is larger at the larger active rate point and that the image has higher contrast in the pixels with gray values having larger active rates.

In addition to ROI mapping, for darker or brighter regions, a toe-shoulder LUT construction step was included for additional mapping, such as the toe region and the shoulder region in the LUT curve in figure 4. The toe region was constructed for mapping the dark area in the image, while the shoulder region was constructed for the bright area in the image.

2.4. MTANNs for bone image creation

For bone image creation, the MTANN (Suzuki *et al* 2006) comprised a machine-learning regression model such as a linear-output multilayer ANN regression model, which is capable of operating directly on pixel data. This model employs a linear function instead of a sigmoid function as the activation function of the unit in the output layer. This was used because the

characteristics of an ANN have been shown to be significantly improved with a linear function when applied to the continuous mapping of values in image processing.

The MTANN involves training with massive sub-region-pixel pairs, which we call a massive-sub-region training scheme. For bone suppression, CXRs are divided pixel by pixel into a large number of overlapping sub-regions (or image patches). Single pixels corresponding to the input sub-regions are extracted from the teaching images as teaching values. The MTANN is massively trained by using each of a large number of input sub-regions (or patches) together with each of the corresponding teaching single pixels. The inputs to the MTANN are pixel values in a sub-region (or an image patch), R extracted from an input image. The output of the MTANN is a continuous scalar value, which is associated with the center pixel in the sub-region, represented by

$$O(x,y) = \mathrm{ML}\{I(x-i,y-j)\big|(i,j)\in R\}, \tag{5}$$

where ML(·) is the output of the machine-learning regression model and *I(x,y)* is a pixel value of the input image. The error to be minimized by training of the MTANN is represented by

$$E = \frac{1}{P}\sum_{c}\sum_{(x,y)\in R_T}\{T_c(x,y) - O_c(x,y)\}^2, \tag{6}$$

where c is the training case number, O_c is the output of the MTANN for the cth case, T_c is the teaching value for the MTANN for the cth case, and P is the number of total training pixels in the training region for the MTANN, R_T.

Although an MTANN was able to suppress the ribs in CXRs (Suzuki *et al* 2006), a single MTANN did not efficiently suppress rib edges, ribs close to the lung wall, and the clavicles, because the orientation, width, contrast, and density of bones differ among locations and because the capability of a single MTANN is limited. To improve the suppression of bones at different locations, we extended the capability of a single MTANN and developed an anatomically specific multiple-MTANN scheme that comprised eight MTANNs arranged in parallel. Each anatomically specific MTANN was trained independently using standard CXRs with the corresponding anatomic segments. The lung field was divided into eight anatomic segments: a left upper segment for suppression of the left clavicles and ribs, a left hilar segment for suppression of the bone in the hilar area, a left middle segment for suppression of the ribs in the middle of the lung field, a left lower segment for suppression of the ribs in the left lower lobe, a right upper segment, a right hilar segment, a right middle segment, and a right lower segment. For each anatomically specific MTANN, the training samples were specifically extracted from the corresponding anatomic segment mask. After training, each of the segments in a non-training ICU CXR was inputted into the corresponding trained anatomically specific MTANN for processing of the anatomic segment in the lung field. For example, MTANNs No.1 was trained to process the left-upper segment in the lung field, which contains the clavicle, and MTANNs No.2 was trained to process the left hilar segment. The eight segmental output sub-images from the anatomically specific multiple MTANNs were then composited to an entire bone image using the eight anatomic segment masks. To blend the sub-images smoothly near their boundaries, anatomic segmentation masks smoothed by a Gaussian filter were used to composite the output sub-images, represented by

$$f_{\mathrm{b}}(x,y) = \sum_{i=1}^{8} O_i(x,y) \times f_{\mathrm{G}}\,[M_i(x,y)], \tag{7}$$

where $f_{\mathrm{b}}(x,y)$ is the composite bone image, O_i is the ith trained anatomically specific MTANN, $f_{\mathrm{G}}(.)$ is a Gaussian filter operator, and M_i is the ith anatomic segmentation mask. In our

Figure 6. Templates used for gray-level morphological enhancement.

experiment, the parameter of sigma for the Gaussian filter was determined to be 10.0, while the size of the template was 9×9 pixels.

For training of overall features in each anatomic segment in the lung field, 10,000 pairs of training samples were extracted randomly from the anatomic segment for each anatomically specific MTANN. A three-layered MTANN was used, where the numbers of input, hidden, and output units were 81, 20, and 1, respectively. Once the MTANNs are trained, the dual-energy imaging system is no longer necessary. The trained MTANNs can be applied to ICU CXRs for suppression of bones. The advantages of this technology over real dual-energy imaging are that there is no need for special equipment to produce dual-energy images, or no additional radiation dose to patients.

2.5. Bone image processing and soft tissue image creation

In the improved bone suppression method, a total variation (TV) minimization smoothing method, which was first introduced into the context of image smoothing by Rudin (Rudin *et al* 1992), was applied to the bone image, following which the smoothed bone image is subtracted from the original CXR to obtain a soft tissue image. For ICU CXRs, the bone image showed more noise and lower contrast of bones than for standard CXRs. A bone structure enhancement method based on the gray-level morphology theory was applied in our scheme.

We applied five gray-level morphologic opening operators with line templates to post-process the bone image. Five rib templates with five different orientations, i.e.,-45, -22, 0, $+22$, and $+45$ degrees, as shown in figure 6, were used for enhancing rib-like structures and eliminating other structures. The size of each template is 17×17 pixels. For each template image b_i in figure 6, the enhanced image is expressed as following:

$$f_{\text{temp}}(s,t) = \min\{f_b(s+x, t+y) - b_i(x,y) \,|\, (s+x), (t+y) \in D_{f_b}; (x,y) \in D_{b_i}\} \tag{8}$$

$$f_{\text{en}-i}(s,t) = \max\{f_{\text{temp}}(s-x, t-y) + b_i(x,y) \,|\, (s-x), (t-y) \in D_{f_{\text{temp}}}; (x,y) \in D_{b_i}\} \tag{9}$$

where: $f_b(x,y)$ is the bone image. $b_i(x,y)$ is the rib template in figure 6. D_{f_b}, $D_{f_{\text{temp}}}$, and D_{b_i} are the domains of f_b, f_{temp}, and b_i, respectively. Then the maximum value among the outputs of the five operators was stored in each pixel in the enhanced bone image.

$$f_{\text{enhanced}}(x,y) = \max_{i=1,2,3,4,5} \{f_{\text{en}-i}(x,y)\} \tag{10}$$

After the enhanced bone image was obtained, the soft tissue image could be acquired using the subtraction technique. We focused on suppression of the ribs and clavicles in the lung field regions. For processing only in the lungs, lung segmentation was used, and suppression was performed only in the segmented lungs using the subtraction technique. After segmentation, a Gaussian filter was applied for smoothing the edges of the segmented lung regions to create an image $m(x,y)$ for masking the outside of the lung regions. The masking image was normalized to have values from 0 to 1. For suppression of the ribs in an ICU CXR, the bone image $f_b(x,y)$

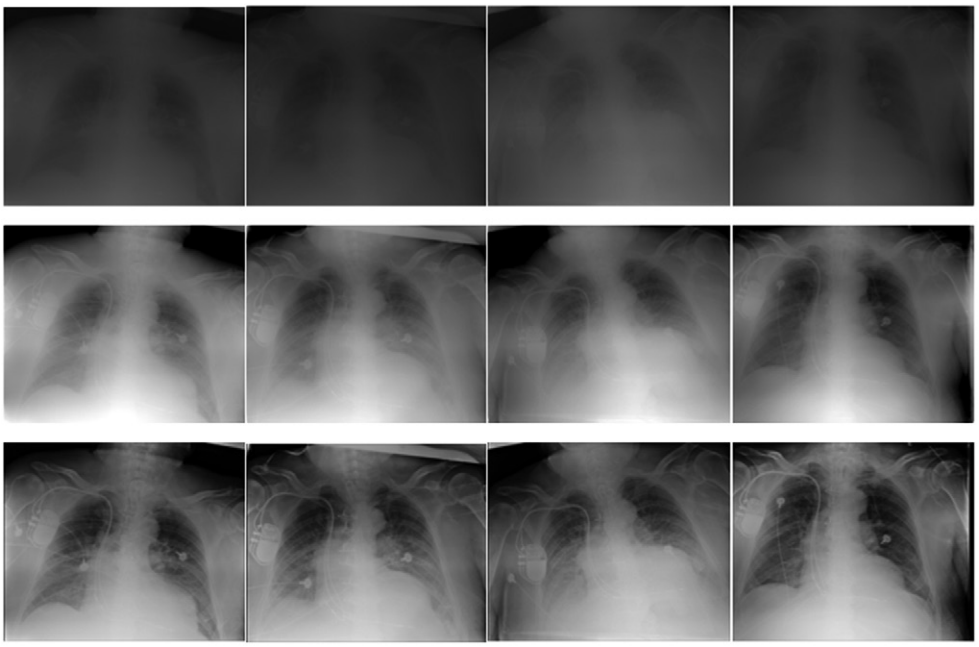

Figure 7. Consistent processing for 4 ICU CXRs from same patient, first column: the first image with the corresponding processed images; second column: the second image with the corresponding processed images; third column: the third image with the corresponding processed images; fourth column: the fourth image with the corresponding processed images; first row: original ICU CXRs from same patient; second row: tone-scale based processed images; third row: consistent processed images.

produced by the anatomically specific multiple MTANN was subtracted from the original CXR *g(x,y)* with the masking image *m(x,y)* as follows:

$$f_S(x,y) = g(x,y) - w_C \times f_b(x,y) \times m(x,y), \tag{11}$$

where w_C is a weighting parameter for determining the contrast of ribs. By changing the weighting parameter w_C, one can obtain processed CXRs with different contrast of ribs and clavicles.

3. Results

In this section, we discuss the results of 87 portable CXRs taken from 20 patients. An evaluation of all 20 patients was performed to compare the overall consistency in the image and the lung areas as well as the ability to detect changes in patients' conditions against the clinician's diagnosis.

3.1. Consistent processing

Consistent processing plays an important role in the detection of subtle changes as well as in bone suppression. Figure 7 shows some examples of consistent processing for four images of a single patient. Although the dose and brightness differ, the contrast is high and the brightness

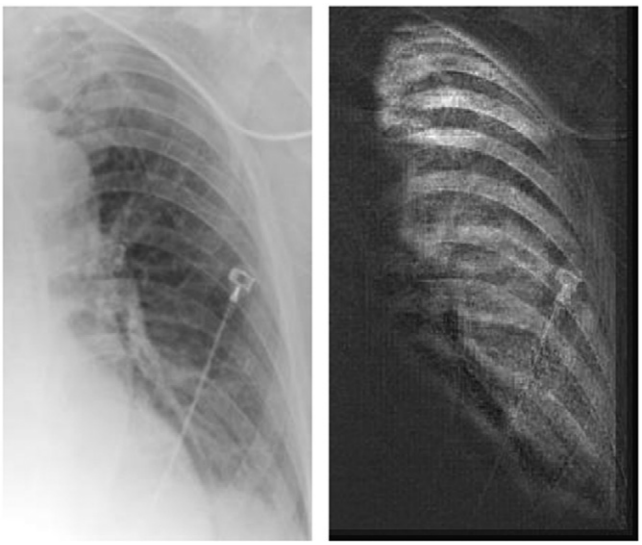

(a) (b)

Figure 8. (a) ICU CXR enhanced by use of consistent processing method; (b) the corresponding bone image created by use of trained MTANN.

is consistent after processing. Clinicians can easily detect cardiomegaly and CHF on these consistent, enhanced images (figure 7(c)).

3.2. Bone image creation

After the ICU CXRs were consistently enhanced by our method, they were inputted into the trained MTANN for the generation of an ICU bone image. Figure 8 shows a bone image processed from an ICU CXR using the trained MTANN. Although the MTANN was trained by standard CXR and the original ICU CXR was totally different from the training image, the bone image still showed high contrast and low noise.

On the other hand, because there are several support devices and a large area of fusion within the lung field on the ICU CXR, and because we never use these patterns for training, the SNR of the bone image for the ICU CXR was lower than that for the standard CXR. For example, the contrast of bones in the upper lung field was lower because there was a large fusion area in the consistent, processed ICU CXR (figure 8). Furthermore, the signal of some support devices with a line structure was strong in the bone image. An orientation-based line structure enhancement method is necessary to enhance the bone structure and suppress noise and other structures on bone images.

3.3. Bone image smoothing and enhancement

As mentioned above, there is a fair amount of noise on bone images. Although the Gaussian filter can smooth the noise, it can also smooth the bone edges. As a result, the bone edges are preserved in the soft image when subtracting the bone image from the corresponding ICU CXR. Here, we introduced the TV minimization noise smoothing method, which can smooth the noise in the bone image while preserving the edge information of bones. The primary

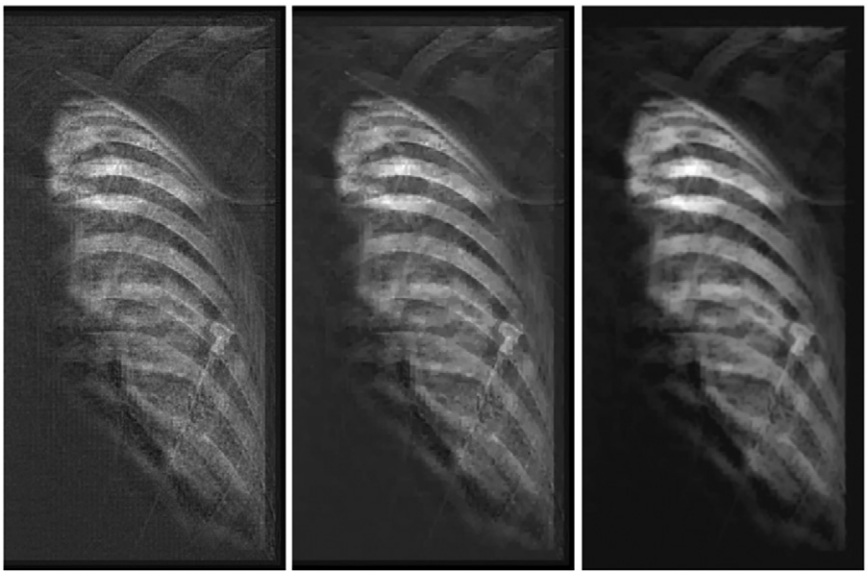

Figure 9. Bone image smoothing and enhancement by use of total variation minimization algorithm and gray scale based morphological opening method, respectively: (a) bone image created from trained MTANN; (b) TV minimization smoothed bone image; (c) enhanced with gray scale morphological method.

advantage of the TV formulation is the ability to preserve bone edges on the images, because of the piecewise smooth regularization property of the TV norm. Figure 9(b) shows the results of bone smoothing. The noise in the bone image was decreased while the bone edge was preserved.

In order to obtain a high SNR and a high-contrast bone image for ICU CXRs and to suppress bone efficiently, the bone contrast should be further enhanced. The gray-scale morphological opening method was used in this study. Because the direction of bones is close to horizontal, we only applied line templates with five different orientations, i.e.,−45, −22, 0, +22, and +45 degrees, for bone enhancement. As shown in figure 9(c), the bone contrast is enhanced using the gray-level morphological opening method, while the supporting device, which is close to the vertical direction, is suppressed in the bone image.

3.4. Performance of consistent processing and bone suppression

In order to prove the objective superiority of our proposed algorithm, we applied the measurement of enhancement by entropy evaluation (EMEE) to evaluate our processed image (Agaian *et al* 2000). EMEE is the most commonly used image processing evaluation standard at present, and an effective measure to evaluate image enhancement quality. It is calculated by dividing an image $I(i, j)$ into $k1 \times k2$ blocks to obtain the local maximum $I(I_{\max;k,l})$ and minimum $(I_{\min;k,l})$ within each block. The following equation is then applied to calculate the EMEE value. For CXRs in our experiment databases, the intensity of pixels ranged from 0 to 4095, with many pixels having an intensity of 0. Thus, the nonzero constant, c, was added to avoid obtaining a zero in the denominator in the following equation. In our experiment, c was set to 5, 20, and 40, and the results were compared.

Table 2. EMEE evaluation of the study database.

EMEE	Original image	Tone-scale	Consistent processing	Bone suppression
$C = 5$	30.9	100.6	181.2	180.7
$C = 20$	19.5	61.2	113.8	111.6
$C = 40$	11.0	33.9	62.0	61.9

Table 3. The evaluation results.

	Clinician 1 (score)				Clinician 2 (score)				Clinician 3 (score)			
Patient number \ Processing method	T	C	C	B	T	C	C	B	T	C	C	B
1	4	4	4	4	4	5	5	5	4	5	5	5
2	3	4	4	5	4	5	5	5	3	4	4	4
3	4	5	5	5	3	4	4	4	5	5	5	5
4	3	4	4	4	3	4	4	5	2	3	3	3
5	5	5	5	5	5	5	5	5	4	5	5	5
6	4	5	5	5	4	5	5	5	4	5	5	5
7	2	3	3	4	3	4	4	4	3	4	4	4
8	2	2	2	4	2	3	3	4	2	3	3	3
9	5	5	5	5	5	5	5	5	4	5	5	5
10	4	5	5	5	4	5	5	5	4	5	5	5
11	4	4	4	4	3	4	4	5	4	4	4	4
12	4	5	5	5	4	5	5	5	5	5	5	5
13	3	4	4	4	3	4	4	4	3	4	4	4
14	4	5	5	5	3	4	4	4	4	5	5	5
15	4	5	5	5	5	5	5	5	4	5	5	5
16	4	5	5	5	4	5	5	5	3	4	4	5
17	3	4	4	4	4	5	5	5	4	4	4	4
18	3	4	4	5	2	3	3	4	4	5	5	5
19	3	4	4	4	3	4	4	4	3	4	4	4
20	2	3	3	4	3	4	4	4	2	3	3	4
Non parametric test (Wilcoxon Signed Rank test) Sig.	0.000		0.034		0.000		0.046		0.000		0.157	

T: Tone-scale based method.
C: Consistent processing without bone suppression.
B: Consistent processing with bone suppression.

$$\mathrm{EMEE} = \frac{1}{k1 \times k2} \sum_{l=1}^{k2} \sum_{k=1}^{k1} \frac{I_{\max;k,l}}{I_{\min;k,l} + c} \log \frac{I_{\max;k,l}}{I_{\min;k,l} + c} \tag{12}$$

Table 2 shows the EMEE results for images processed by using our method as well as the original images and those processed by using tone-scale method. We chose block size 40×40, with $c = 5$, $c = 20$, and $c = 40$, respectively. Larger EMEE values indicate better enhancement performance. From the results, we found that the proposed consistent processing method performed significantly better in general than tone-scale method. For the bone

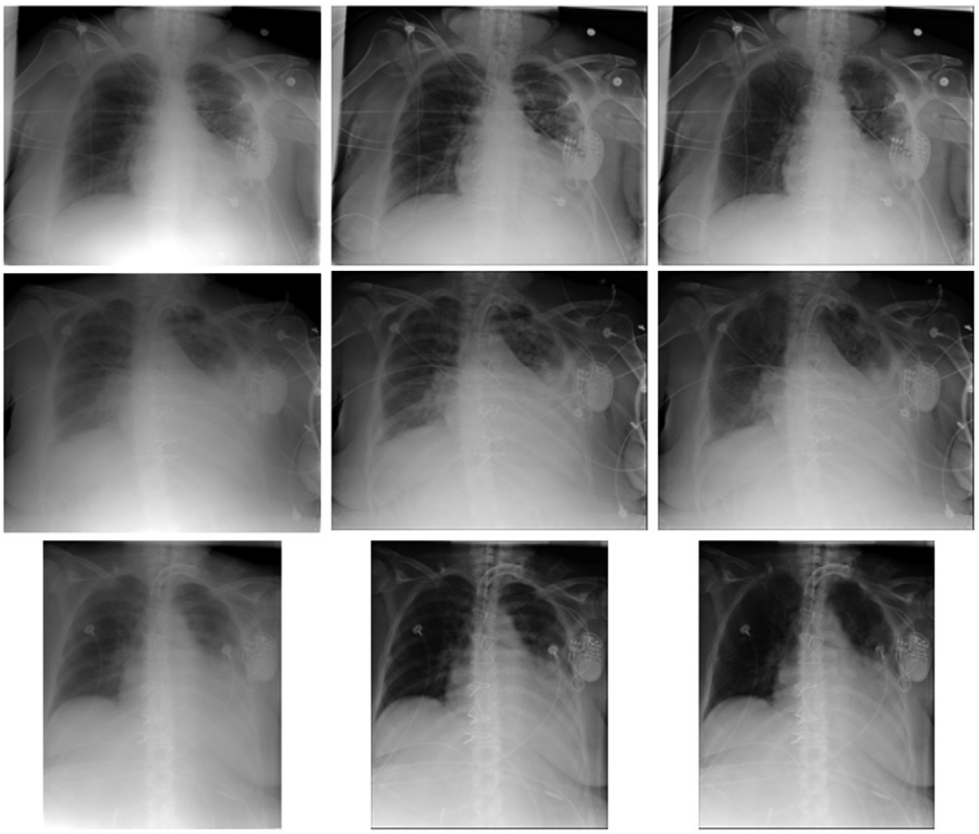

Figure 10. Chest Radiographs enhancement in ICU for same patient, first column: tone-scale processed CXRs in ICU; second column: consistent processing results; third column: bone suppression; first row: the first image with the corresponding processed images; second row: the second image with the corresponding processed images; third row: the third image with the corresponding processed images.

suppression images, the EMEE value was comparable to those before bone suppression. It proved that our bone suppression technique did not import noise or reduce the quality of the image.

A subjective evaluation method was also proposed by three expert ICU clinicians. They provided ratings on a 5-point acceptability scale, where '1' is not acceptable and '5' is outstanding in terms of the enhancement effect among the images presented for diagnostic purposes. Three methods for the enhancement of ICU CXRs were compared (traditional tone-scale method, our consistent processing method without bone suppression, and our consistent processing method with bone suppression). Table 3 shows the evaluation results. *The test values tell us that the consistent processing without bone suppression method substantially improved the 5-point score for all three clinicians comparing to the tone-scale based method. Furthermore, the consistent processing with bone suppression method improved the 5-point score for both clinician 1 and clinician 2.* The consistent, processed image with bone suppression improved the confidence of clinicians' and aided in the interpretation of ICU CXRs with more effectiveness and efficiency. All three clinicians provided scores for each of the 20 patients using the consistent, processed images with bone suppression.

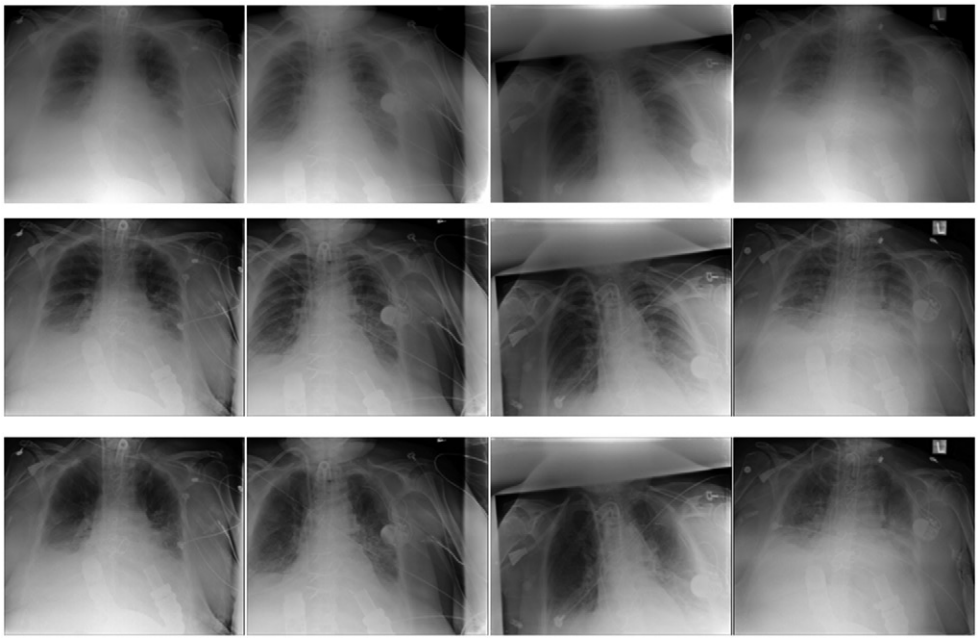

Figure 11. Chest radiographs enhancement in ICU for same patient, first column: the first image with the corresponding processed images; second column: the second image with the corresponding processed images; third column: the third image with the corresponding processed images; fourth column: the fourth image with the corresponding processed images; first row: tone-scale processed CXRs in ICU; second row: consistent processing results; third row: bone suppression.

Figure 10 shows a patient's ICU CXRs. For this patient, clinicians were required to evaluate the working status of a pacemaker and determine whether abnormalities could arise after the removal of a peripherally inserted central catheter. The evaluation scores for our method with regard to this patient were 5. Using the enhanced images, clinicians could easily observe that the tube at the top of the patient is external to the patient and that there is a pacemaker with short wires. CHF decreased for this patient. Figure 11 shows a patient with a chest tube introduced on the right side for the drainage of pneumothorax. The radiologist gave a score of 5 for the processing results because it was easier to evaluate the status. Using this consistent method, the differences in the lungs were decreased, and it was easier to evaluate CHF (figure 11).

4. Conclusion and discussion

We have developed a consistent processing and bone suppression method to decrease variations in image appearance and improve the diagnostic quality of images. With our new technique, clinicians can improve their ability to characterize the lung parenchyma and subtle pathological changes and increase their confidence in making diagnosis regarding the presence or absence of an abnormality on ICU CXRs.

The interpretation of chest radiographs is very challenging. The appearances or characteristics of various lung diseases vary dramatically in terms of size, shape and contrast. It is critical that a bone suppression method is capable of preserving the image details so that the SNR can be improved for a range of lung diseases after bone suppression. We expect this method to

provide ICU clinicians with a means to enhance their interpretation of CXRs with improved effectiveness and efficiency.

In this study, the bone suppression parameters were fixed. However, we can optimize the suppression by use of different parameters for CXRs obtained using different exposure settings. The parameters used for consistent processing were determined from the nine training standard CXRs and validated by an empirical radiologist. In the future, we will work towards optimizing these parameters.

The bones were not satisfactorily suppressed in some images, probably because the proposed method only suppressed the bone in the segmented lung field. Segmentation on ICU CXRs is a difficult task. Although we have introduced the improved active shape model (ASM) for lung segmentation, it failed for some images with large fusion areas in the lung field because the local features used for matching with lung boundaries were totally different from those on standard CXRs. Furthermore, the lung shape on ICU CXRs may be largely deviated from the shape model trained by the standard CXR. The performance of lung segmentation has the potential to be improved in our future work.

The time for processing one image with our enhancement method was 7.1 s (including 5.5 s for image consistent processing and 1.6 s for bone suppression) on a PC-based workstation (Intel Pentium 2.4 GHz processor with a 3 GB memory). Consistent processing consumed most of the processing time because there are background segmentation and ROI automatic selection steps in consistent processing. Bone suppression is almost real time and software can be applied prior to interpretation for every image without any delay, thus satisfying the clinical requirement.

Acknowledgements

This work was supported by the National Science Foundation of China (NSFC) 81101116, the Foundation of Hujiang (C14002), and the National Sciences Foundation of Shanghai (13ZR1410400). The authors declare that they have no conflict of interest. All procedures performed in studies involving human participants were in accordance with the ethical standards of the institutional and national research committee and with the 1964 Helsinki declaration and its later amendments or comparable ethical standards. Informed consent was obtained from all individual participants included in the study. Computer-aided diagnosis and machine learning technologies developed at the University of Chicago have been licensed to companies including R2 Technology, Riverain Medical, AlgoMedica, Deus Technology, Median Technologies, Mitsubishi Space Software, and General Electric.

References

Agaian S *et al* 2000 A new measure of image enhancement *Int. Conf. of Signal Processing (Marbella, Spain)*

Ahmed B and Rasheed T 2007 Rib suppression for enhancing frontal chest radiographs using independent component analysis *Lecture Notes Comput. Sci.* **4432** 300–8

Amorosa J K *et al* 2013 ACR appropriateness criteria routine chest radiographs in intensive care unit patients *J. Am. Coll. Radiol.* **10** 170–4

Chahine-Malus N *et al* 2001 Utility of routine chest radiographs in a medical-surgical intensive care unit: a quality assurance survey *Crit. Care* **5** 271–5

Chen S and Suzuki K 2013 Computerized detection of lung nodules by means of virtual dual-energy radiography *IEEE Trans. Biomed. Eng.* **60** 369–78

Chen S and Suzuki K 2014 Separation of bones from chest radiographs by means of anatomically specific multiple massive-training ANNs combined with total variation minimization smoothing *IEEE Trans. Med. Imaging* **33** 246–57

Chen S Y and Zou L 2009 Chest radiographic image enhancement based on multi-scale retinex technique *2009 3rd Int. Conf. Bioinformatics and Biomedical Engineering* vols 1–11 pp 2036–8

Ely E W *et al* 2001 Radiologic determination of intravascular volume status using portable, digital chest radiography: a prospective investigation in 100 patients. *Crit. Care Med.* **29** 1502–12

Hammon M *et al* 2014 Improving diagnostic accuracy in assessing pulmonary edema on bedside chest radiographs using a standardized scoring approach *BMC Anesthesiol.* **14** 94

Hogeweg L *et al* 2013 Suppression of translucent elongated structures: applications in chest radiography *IEEE Trans. Med. Imaging* **32** 2099–113

Ishigaki T *et al* 1986 One-shot dual-energy subtraction imaging *Radiology* **161** 271–3

Ishigaki T *et al* 1988 One-shot dual-energy subtraction chest imaging with computed radiography: clinical evaluation of film images *Radiology* **168** 67–72

Loog M *et al* 2006 Filter learning: application to suppression of bony structures from chest radiographs *Med. Image Anal.* **10** 826–40

Mercan C A and Celebi M S 2014 An approach for chest tube detection in chest radiographs *IET Image Process.* **8** 122–9

Murphy G P *et al* 1995 *American Cancer Society textbook of Clinical Oncology* (Atlanta, GA: The Society)

Oda S *et al* 2009 Performance of radiologists in detection of small pulmonary nodules on chest radiographs: effect of rib suppression with a massive-training artificial neural network *AJR Am. J. Roentgenol.* **193** W397–402

Plourde F *et al* 2012 Semiautomatic detection of scoliotic rib borders from posteroanterior chest radiographs *IEEE Trans. Biomed. Eng.* **59** 909–19

Reyes G *et al* 2001 Use of an optical fiber scope to confirm endotracheal tube placement in pediatric patients *Crit. Care Med.* **29** 175–7

Rudin L I *et al* 1992 Nonlinear total variation based noise removal algorithms *Physics* D **60** 259–68

Ryoo J *et al* 2013 Real-time implementation of an LUT-based image warping system. Robotics(ISR) *2013 44th Int. Symp. on, IEEE*

Stewart B K and Huang H K 1990 Single-exposure dual-energy computed radiography *Med. Phys.* **17** 866–75

Strain D S *et al* 1985 Value of routine daily chest x-rays in the medical intensive care unit *Crit. Care Med.* **13** 534–6

Suzuki K 2012 Pixel-based machine learning in medical imaging *Int. J. Biomed. Imaging* **2012** 18

Suzuki K, Abe H, Li F and Doi K 2004 Suppression of the contrast of ribs in chest radiographs by means of massive training artificial neural network *Proc. SPIE Medical Imaging (SPIE MI)* **5370** 1109–19

Suzuki K *et al* 2006 Image-processing technique for suppressing ribs in chest radiographs by means of massive training artificial neural network (MTANN) *IEEE Trans. Med. Imaging* **25** 406–16

Wandtke J C 1994 Bedside chest radiography *Radiology* **190** 1–10